BNL-224202-2023-JAAM

Atomistic Origins of Reversible Noncatalytic Gas-Solid Interfacial Reactions

X. Chen, S. Hwang

To be published in "Journal of the American Chemical Society"

February 2023

Center for Functional Nanomaterials

Brookhaven National Laboratory

U.S. Department of Energy

USDOE Office of Science (SC), Basic Energy Sciences (BES) (SC-22)

DISCLAIMER

Atomistic Origins of Reversible Noncatalytic Gas-Solid Interfacial Reactions

Xiaobo Chen[1‡], Jianyu Wang[1‡], Yaguang Zhu[1], Zhenhua Xie[2], Shuonan Ye[1], Kim Kisslinger[3], Sooyeon Hwang[3], Dmitri N. Zakharov[3], Guangwen Zhou[1*]

[1] Department of Mechanical Engineering & Materials Science and Engineering Program, State University of New York at Binghamton, Binghamton, New York 13902, United States

[2] Chemical Division, Brookhaven National Laboratory, Upton, New York 11973, United States

[3] Center for Functional Nanomaterials, Brookhaven National Laboratory, Upton, New York 11973, United States

Abstract

Noncatalytic gas-solid reactions are a large group of heterogeneous reactions that are usually assumed to occur irreversibly because of the strong driving force to favor the forward direction toward the product formation. Using the example of Ni oxidation into NiO with CO_2, herein we demonstrate the existence of the reverse element that results in the NiO reduction from the countering effect of the gaseous product of CO. Using in-situ electron microscopy observations and atomistic modeling, we show that the oxidation process occurs via preferential CO_2 adsorption along step edges that results in step-flow growth of NiO layers, and the presence of Ni atoms on the flat NiO surface promotes the nucleation of NiO layers. Simultaneously, the NiO reduction happens via preferential step-edge adsorption of CO that leads to the receding motion of atomic steps, and the presence of Ni vacancies in the NiO surface facilitates the CO adsorption induced surface pitting. Based on the in-situ TEM observations, temperature and CO_2 pressure effect maps are constructed to illustrate the spatiotemporal dynamics of the competing NiO redox reactions. These results demonstrate the rich gas-solid surface reaction dynamics induced by the co-existing forward and reverse reaction elements and have practical applicability in manipulating gas-solid reactions via controlling the gas environment or atomic structure of the solid surface to steer the reaction toward the desired direction.

‡These authors contributed equally to the work.

* To who correspondence should be addressed: gzhou@binghamton.edu

Introduction

Noncatalytic gas-solid reactions are of considerable industrial importance and are readily found in chemical and metallurgical industries. Examples include the oxidation of metals or the reduction of metal oxides, the combustion of solid fuels and solid propellants, the gasification of coal, and the regeneration of catalysts, among others.[1–6] In general, they are usually extremely complex, and experiments performed to estimate the intrinsic kinetics can easily fail to reveal the true mechanism. This is because of the large number of variables involved, including the complex mixed gas atmospheres, transfer of gas molecules to the solid surface, chemical reaction at the gas/solid interface, and changes in size, shape and microstructure of the solid surface during the reaction and product formation on the solid.[2-12] Particularly, the chemical reaction at the gas-solid interface is a critical step in determining the rate law for the overall reaction and is usually assumed to occur irreversibly because the equilibrium is totally shifted to the reaction products.[7–10] Herein, we demonstrate that this assumption of the irreversibility is oversimplified, and conditions exist for the reverse element of the reaction to occur, even for the simple case with a pure feeding gas to strongly favor the forward direction of the reaction.

Our work is based on real-time atomic-scale observations of the oxidation of metallic Ni into NiO in a CO_2 atmosphere. This is performed with the use of dedicated environmental transmission electron microscopy (TEM) to flow CO_2 gas in the sample area to activate the reaction between CO_2 and Ni at elevated temperature while at the same time temporally and spatially resolving the dynamic evolution of local atomic configurations at the gas-solid interface. Our interest in the CO_2-Ni reaction system stems from its technological importance, including CO_2 capture and utilization through its conversion into value-added chemicals (CO, methane, methanol and hydrocarbon)[11–17] and high-temperature corrosion of structural alloys used in next-generation power cycles that use supercritical CO_2 as the working fluid to obtain high conversion efficiency (> 50%).[18–21] With the in-situ atomistic observations, we capture the simultaneously occurring forward reaction of NiO growth and backward reaction of NiO reduction under the condition far from the chemical equilibrium. This phenomenon has not been recognized due to the difficulty of probing the fast dynamics of the local atomic configurations of the gas-solid interface under the reaction conditions of elevated temperature and pressure. By combining the in-situ microscopic observations with density-functional theory (DFT) simulations, we identify the atomistic mechanism by which the surface defects

of atomic vacancies and ledges regulate the forward and reverse reactions. The phenomenon shown here has wide relevance and is of considerable practical importance, as the existence of the reversible steps is expected to result in large departure from the prediction by the irreversible assumption of the rate of the overall conversion for a wide range of noncatalytic gas-solid reactions.

Results and Discussion

2.1 In-situ environmental TEM observations

In-situ TEM imaging is used to monitor the surface evolution of Ni during the CO_2 exposure and shows that the surface reaction is dominated by NiO growth (see Fig. S1 captured from in-situ TEM video 1). However, some local areas exhibit simultaneous NiO growth and reduction, and Fig. 1 illustrates time-sequence HRTEM images (captured from supporting in-situ TEM Movie 2) revealing such an instance while exposing Ni at T = 450 °C to ≈ 4×10^{-5} Torr of CO_2 gas flow. As seen in Fig. 1(a), the Ni oxidation in CO_2 results in NiO grain growth, where the two NiO grains have the zone axes of [001] and $[01\bar{1}]$ and form a V-shape grain-boundary groove with the exposed {100} facets. The (100) facet on the left is atomically flat whereas the (100) facet on the right is defective with presence of monoatomic steps, as outlined by the dashed white and cyan lines, respectively. As shown in Fig. 1(b), a monoatomic layer (numbered 1) nucleates at the corner of the flat (100) facet of the grain on the left, and this results in a step-terrace configuration. The step is observed to sweep laterally via the step-flow NiO growth by the attachment of O and Ni adatoms to the step edge, where O atoms are supplied from the dissociative adsorption of CO_2 molecules in the surrounding gas phase ($CO_2 \rightarrow CO + O$) whereas the Ni atoms are either from the Ni substrate via the outward diffusion or from the NiO reduction of the neighboring NiO grain, as supported by DFT-calculated Ni diffusion energy barrier of 0.28 eV in Fig. S2. As seen in Figs. 1(b-d), this step-flow NiO growth results in the formation of a complete atomic layer on the (100) facet. Figs. 1(e, f) illustrate that monoatomic layers can also nucleate at the two corner regions (numbered 2, 3) of the flat (100) facet of the left grain. These atomic layers propagate toward each other via step-flow growth and their perfect merging leads to the growth of a complete new atomic layer (Fig. 1(f)). Fig. 1(g) shows that the nucleation of a monoatomic layer (numbered 4) can also takes place in the middle of the flat (100) terrace of the left grain, where the step-flow growth of the two atomic steps in the opposite directions results in the formation of a new atomic layer of NiO (Figs. 1(h, i)).

In contrast to the step-flow, layer-by-layer oxide growth on the flat (100) facet, the defective (100) facet of the neighboring NiO grain shows the reverse reaction of the oxide reduction in the same CO_2 atmosphere. The

dashed cyan lines in Figs. 1(a-h) are used to track the locations of the atomic steps, revealing that the NiO grain on the right undergoes the reduction reaction by the retraction motion of the atomic steps and inward nucleation of new monoatomic steps along the (100) facet. As marked by the red arrow in Fig. 1(h), the retraction motion of the monoatomic steps results in the bunching of the atomic steps into a microfacet that is perpendicular to the (100) facet and slows down the oxide reduction. Detailed tracing of the temporal evolution of the surface profile is presented in Fig. 1(i), showing the oxidation reaction on the flat (100) facet on the left that results in the growth of three complete atomic Ni-O layers whereas the oxide reduction on the defective (100) facet on the right that leads to the decay of multiple Ni-O layers from the surface. The red dotted lines in Fig. 1 mark the growth front of an NiO overlayer on the planar surface, which also shows oscillatory forward and backward motion as a result of the coexisting oxide growth and reduction along the step edge. As marked by the red dotted lines in Fig. 1(b) and seen in Supplementary in-situ TEM Movie 2, the surface-like mobile species is visible, which can be related to the dynamic motion of the growth front of the NiO overlayer that is observed to grow and shrink laterally on the planar surface region and momentarily extending into the vacuum. In general, the in-situ TEM imaging does not show obvious buildup of mobile surface species in front of surface steps. This is probably because of the extremely fast rates of step-edge attachment and detachment that lead to the quick depletion of Ni adatoms in front of surface steps. By contrast, terrace regions away from the surface steps show a relatively longer lifetime of Ni adatoms that display fast aggregation and disaggregation dynamics before being trapped by surface steps. This is captured by in-situ TEM imaging (Supplementary in-situ TEM Movie 3) and shown in Fig. S3.

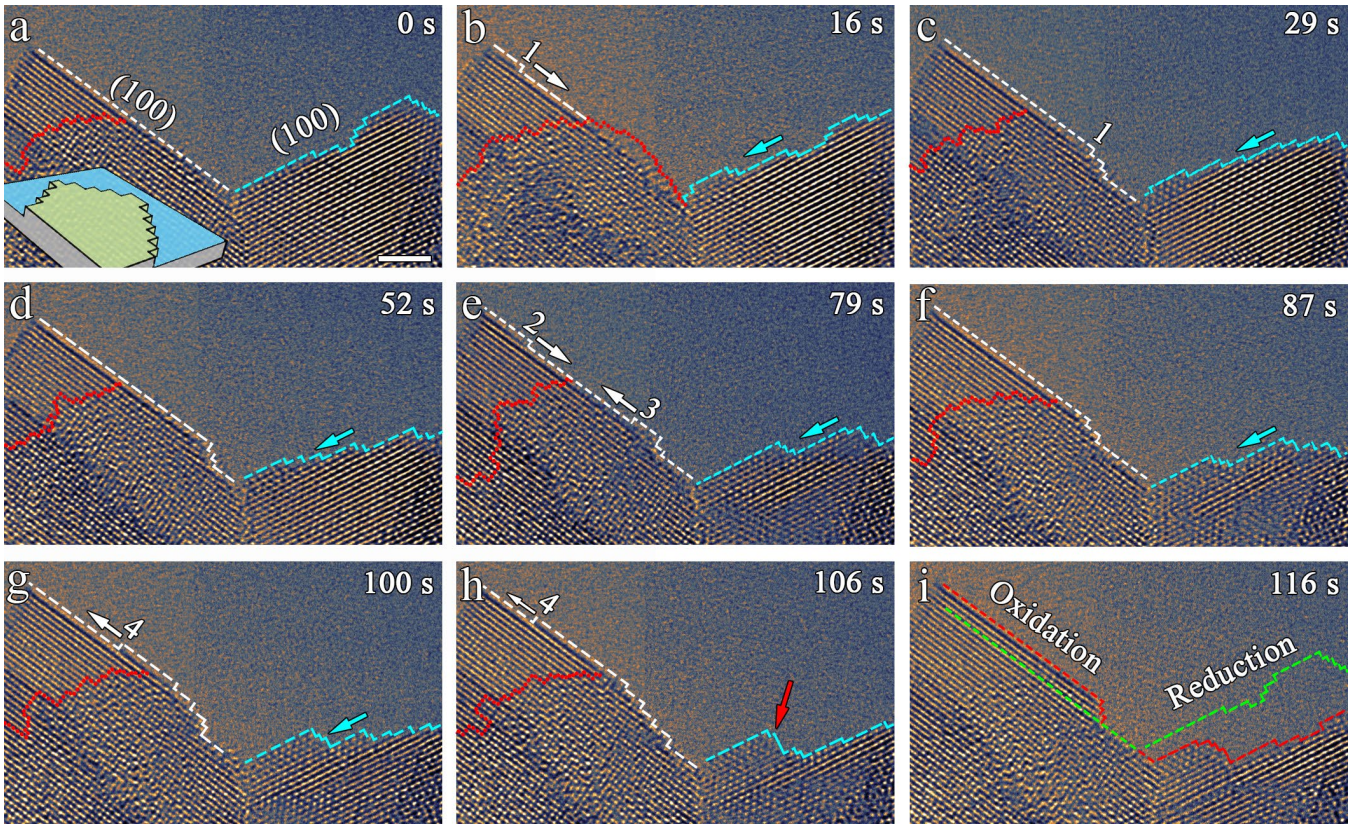

Figure 1. In-situ atomic-scale imaging of the simultaneous oxide growth and reduction at a grain-boundary groove of NiO during the Ni oxidation at 450 ℃ and ≈ 4×10^{-5} Torr of CO_2 gas flow. **a-i** Time-sequence HRTEM images (Supplementary Movie 2) showing the forward reaction of oxide formation via the step-flow oxide growth on the flat (100) facet on the left whereas the reverse reaction of oxide reduction via the retraction motion of atomic steps on the defective (100) facet on the right. The inset in (a) is a schematic view of the presence of atomic steps on the planar surface. The dashed white and cyan lines in (a-h) outline the evolution of the surface profile of the two NiO grains. The green and red dashed lines in (i) are the traces of the position and configuration of the outmost surface facets of the grain boundary groove at 0 s and 116 s, respectively, showing the oxide growth on the left grain whereas the oxide reduction on the right grain. Red dotted lines in (a-h) mark the growth front of an NiO overlayer on the planar surface. Scale bar, 2 nm **a-i**.

The observed simultaneous reactions of the oxide growth and reduction in CO_2 are not tied to separate NiO grains but also occurs on the different surface facets of the same NiO grain, and Fig. 2 depicts such an example (snapshots from in-situ TEM Movie 4). As shown in Fig. 2(a), the (100) side facet of the NiO island is atomically flat whereas the top (100) facet consists of multiple atomic steps. The oxidation reaction occurs on the flat (100) facet, as indicated by the nucleation and step-flow growth of two monoatomic steps (numbered 1 and 2 in Fig. 2(b)). The two atomic steps are observed to propagate toward each other and merge into a complete atomic layer of NiO (Fig. 2(c)). A new monoatomic layer nucleates in the middle of the grown layer, and this results in two new atomic steps (numbered 3, 4 in Fig. 2(d)) that propagate laterally to form another complete atomic layer of NiO (Fig. 2(e)).

This process of nucleating monoatomic layers of NiO and the lateral step-flow growth repeats itself and leads to the layer-by-layer growth of multiple atomic layers of NiO along the side (100) facet (Fig. 2(f-i)). By contrast, the highly stepped (100) facet on the top undergoes the oxide reduction reaction. This is indicated in Figs. 2(a-i), showing the lateral retraction motion of steps and inward nucleation and lateral decay of new atomic steps. Figs. 2(c, d) show the HRTEM images that illustrate the nucleation of two new atomic steps (marked by the cyan arrow) by surface pitting at the flattened terrace and their lateral retraction motion. As shown by the detailed tracing of the temporal evolution of the surface profile in Fig. 2(i), the oxidation reaction on the flat side (100) facet results in the growth of four complete atomic layers of Ni-O layers whereas the oxide reduction on the top defective (100) facet leads to the NiO reduction by a thickness of ~ 2 nm. Also shown by the inset schematic in Fig. 2(a), surface steps are also present on the planar surface region, where the location of the step edge is visible as a slight change in the image contrast due to the difference in thickness across the lower and upper sides of the step edge. Detailed tracing of the positions of the step edge at different times shows the oscillatory forward and backward movement of the step edge on the planar surface.

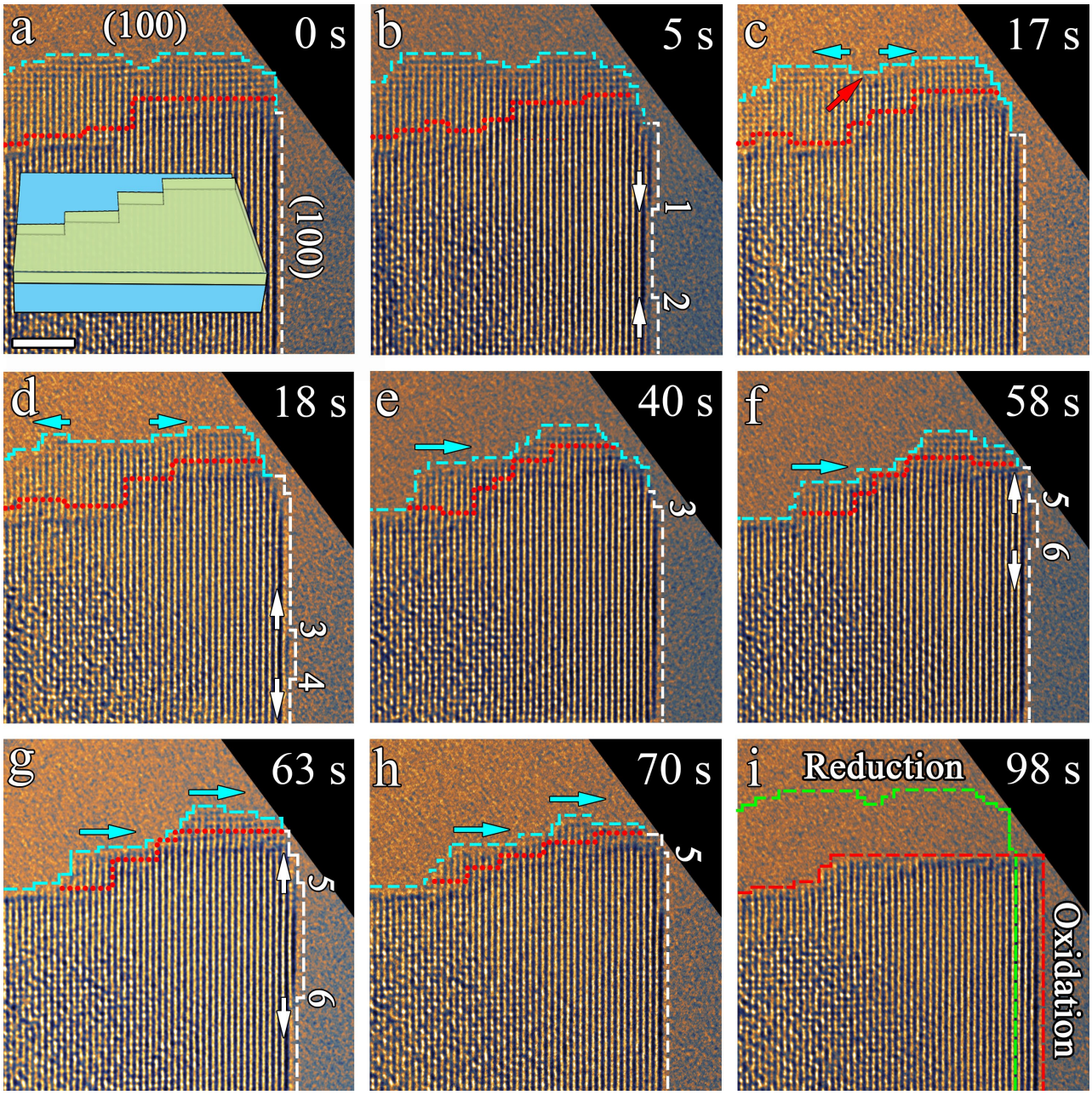

Figure 2. In-situ TEM visualization of the oxide growth and decomposition of a single NiO grain during the exposure of Ni at 450 °C to ≈ 4×10^{-5} Torr of CO_2 gas flow**. a-i** In-situ HRTEM images (Supplementary Movie 4) displaying the layer-by-layer oxide nucleation and growth on the flat (100) side facet whereas the oxide reduction on the top, stepped (100) facet via the retraction motion of atomic steps. The inset in (a) is a schematic illustrating the presence of atomic steps on the planar surface. The red arrow in (c) marks the nucleation of a monoatomic deep surface pit that results in the formation of two monatomic steps. The red dotted lines in (a-h) are the detailed traces of the stepped features on the planar surface. The green and red dashed lines in (i) are the traces of the position and configuration of the outermost surface facets at 0 s and 98 s, respectively, showing the oxide growth on the flat side facet whereas the oxide reduction on the top rough facet. Scale bar, 2 nm **a-i**.

Fig. 3 illustrates time-sequence HRTEM images (extracted from in-situ Movie 5) that demonstrate that the competing oxide growth and decomposition can also take place on the same NiO surface in the CO_2 atmosphere. As shown in Figs. 3(a, b), a monoatomic oxide layer nucleates on an initially atomically flat NiO(100), which results in two monoatomic steps (numbered 1 and 2). The step-flow propagation of the two atomic steps in the opposite directions results in the growth of a new atomic layer of NiO (numbered i in Figs. 3(b-e)). As seen in Fig. 3(f), a new monoatomic step (numbered 3) enters the field of view from the left side, and this results in a step-and-terrace surface configuration. Similarly, the lateral flow of the surface step leads to the growth of another new atomic layer of NiO (numbered ii in Figs. 3(f-i)). As shown in Figs. 3(h, i), this newly formed surface layer shows much weaker lattice image contrast than that of the atomic planes below the surface, indicating its smaller thickness and/or the presence of a high density of atomic defects such as vacancies, steps, and kinks in the topmost layer. This defective surface layer is unstable, and a local area decomposes into a monoatomic deep pit with two newly formed surface steps (numbered 4 and 5 in Fig. 3(i)). Step 4 is observed to undergo the backward motion (induced by the oxide reduction) whereas step 5 experiences the forward motion (induced by the oxide growth). After ~ 3 s, the oxide reduction at step 4 is reverted to the oxide growth while in contrast step 5 still undergoes the oxidation reaction, thereby resulting in the recovery of the oxide layer after the encountering of steps 4 and 5 (Fig. 3(j)). It can be also noted from Fig. 3(k), an atomic layer with the weaker image contrast develops between steps 4 and 5, which has a slightly lower surface height with a smaller interplanar spacing of 1.8 ± 0.1 Å compared to the adjacent NiO(200) lattice spacing and can thus be related to the two-dimensional aggregation of Ni adatoms from the adjacent reducing NiO layer. The presence of metallic Ni can promote the adsorption of CO_2 molecules and facilitate the re-growth of the oxide layer, leading to the recovery of the NiO layer, as shown in Fig. 3(l). By monitoring the evolution of the image contrast as shown in Figs. 3(k, l), it can be seen that the lattice contrast of the two topmost oxide layers grows progressively stronger, indicating the gradual healing of the lattice defects and thickness of the oxide layers. The competing oxide growth and reduction reactions on the same NiO surface are confirmed at multiple places and samples (see more examples in Supplementary Figs. S3, S4).

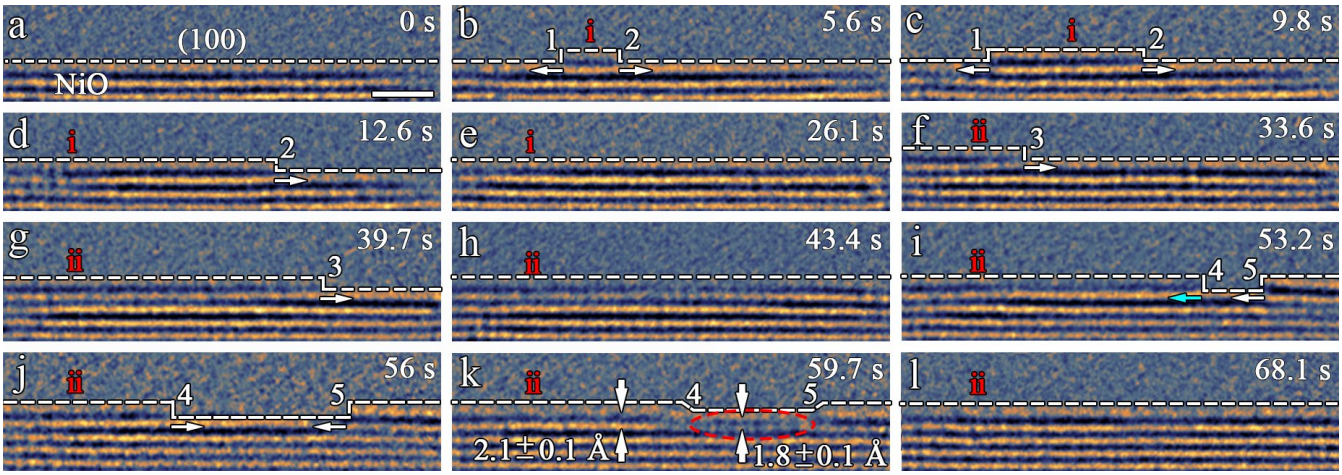

Figure 3. In-situ atomic-scale observations of the competing oxide growth and decomposition on the same NiO(100) surface facet during the Ni oxidation at 450 °C and ≈ 4×10^{-5} Torr of CO_2 gas flow. **a-i** Time-sequence HRTEM images (Supplementary Movie 5) showing a cycle of step-flow oxide growth, oxide reduction via surface pitting at the terrace, and again the step-flow oxide growth leading to the recovery of the topmost NiO layer. The area marked by the red dashed oval shows a smaller interplanar spacing compared to the NiO(200) lattice, indicating the aggregation of Ni adatoms into a metallic-like Ni layer that is subsequently re-oxidized into NiO. Scale bar, 2 nm **a-i**.

Consistent with the above atomic-scale imaging of simultaneous NiO growth and reduction are the in-situ TEM observations of morphological evolution of NiO islands shown in Fig. 4. The initial-stage oxidation processes of metals typically feature the nucleation and growth of oxide nano-islands on the metal surface.[22–26] As shown in Figs. 4(a-f), the areas marked by dashed boxes correspond to NiO islands formed during the Ni oxidation in CO_2. This is confirmed by HRTEM imaging of the oxidized surface, where the regions with NiO islands show moire fringe contrast (marked by dashed circles in Fig. 4(g)) formed as a result of interference between diffracted beams from overlapping NiO islands and the Ni substrate. One obvious feature in the HRTEM image is that moire fringes do not extend continuously to the entire surface, confirming the NiO island growth mode during the early-stage oxidation of Ni in CO_2. Regions between NiO islands have the lattice spacing consistent with the interplanar spacing of Ni{110}. Indexing of the diffractogram (Fig. 4(h)) of the HRTEM image identifies that one set of the reflections is from the Ni<$1\bar{1}2$> substrate and the other is from NiO islands with the epitaxial relationship of $[1\bar{1}2]_{NiO} \parallel [1\bar{1}2]_{Ni}$ and $(220)_{NiO} \parallel (220)_{Ni}$. As seen in Figs. 4(a-f), the image contrast for NiO island 1 becomes gradually weaker, indicating its reduction reaction leading to the oxide decomposition. By contrast, the contrast for island 2 grows darker in the first ~60 s and then becomes weaker afterwards, suggesting the oxide growth and subsequent

reduction to this NiO island. Similarly, the temporal evolution of the image contrast for islands 3 and 4 from growing darker and then weaker is caused by the competing oxidation and reduction reactions of the oxide islands.

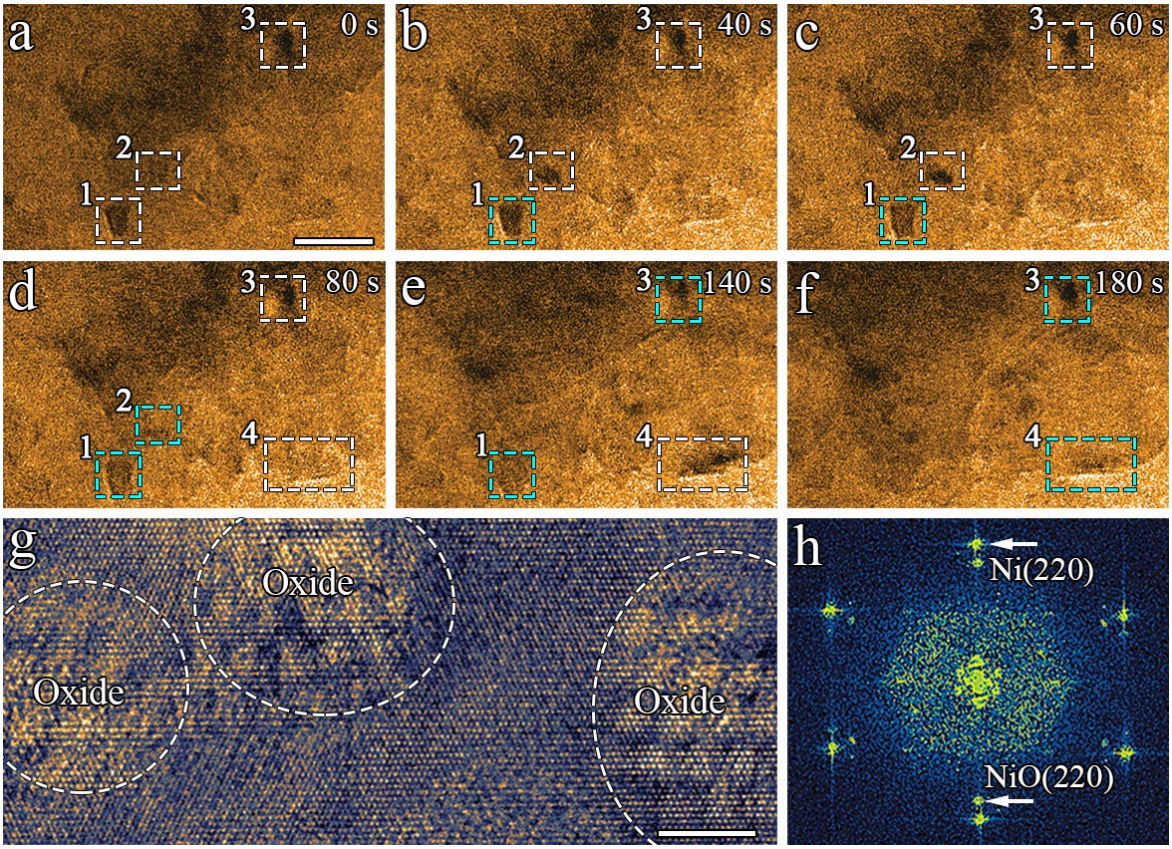

Figure 4. In-situ TEM observations of the morphological evolution of NiO islands during the exposure of Ni at 450 °C to ≈ 4×10^{-5} Torr of CO_2 gas flow. **a-f** Time-sequence low-magnification TEM images (Supplementary Movie 7) showing the growth and shrinkage of NiO islands (marked by dashed white and cyan boxes, respectively) induced by the competing oxide growth and reduction. **g** HRTEM image showing Ni(110) lattice fringes and electron moire fringes due to the lattice superimposition of NiO islands and the Ni substrate. **h** Diffractogram of the HRTEM in (**g**), showing the epitaxial relationship between the NiO and Ni substrate. Scale bar, 10 nm **a-f**, 2 nm **g**.

The effect of temperature and CO_2 pressure on the spatiotemporal evolution of the competing redox dynamics of NiO is also examined with in-situ TEM observations. Figs. 5(a-d) display in-situ HRTEM images showing the forward growth and backward retraction of the oxide layers while exposing Ni at T = 300 °C to ≈ 3×10^{-4} Torr of CO_2 gas flow, where the oscillatory oxide growth and reduction is observed to occur in close proximity (i.e., on the same surface facets). Increasing the temperature to 450 °C (still in ≈ 3×10^{-4} Torr CO_2 gas flow) speeds up the NiO growth and reduction as shown in Figs. 5(e-h), where the competing oxide growth and reduction occurs on two separate facets, indicating a transition of the competing redox dynamics from local areas to the more global

areas. To further demonstrate the influence of CO_2 pressure, Figs. 5(i-l) depict such an example with increasing the CO_2 pressure by two orders of magnitude to $\approx 3\times10^{-2}$ Torr, showing competing NiO growth and reduction on the same facet. By contrast, the higher temperature promotes the transition to the more global redox dynamics, and Figs. 5(m-p) reveal such an instance showing NiO growth on one surface facet whereas NiO reduction on the adjacent facet while exposing Ni at T = 600 ℃ to $\approx 3\times10^{-4}$ Torr of CO_2 gas flow. Based on the in-situ TEM observations performed with the four orders of magnitude difference in CO_2 pressure and temperature varying from 300 to 600 ℃, the temperature and CO_2 pressure effect maps are constructed, respectively. Fig. 5(q) corresponds to the temperature effect, showing that the increase of temperature (at 3×10^{-4} Torr CO_2) results in the transition of the competing oxide growth and reduction dynamics from localized surface areas to a more global scale of the mass transport. By contrast, the increase of the CO_2 pressure from $\sim 4\times10^{-5}$ Torr to $\sim 3\times10^{-2}$ Torr at 450 ℃ leads to the opposite trend of the transition from the global to more local mass transport of the spatiotemporal redox dynamics (Fig. 5(r)).

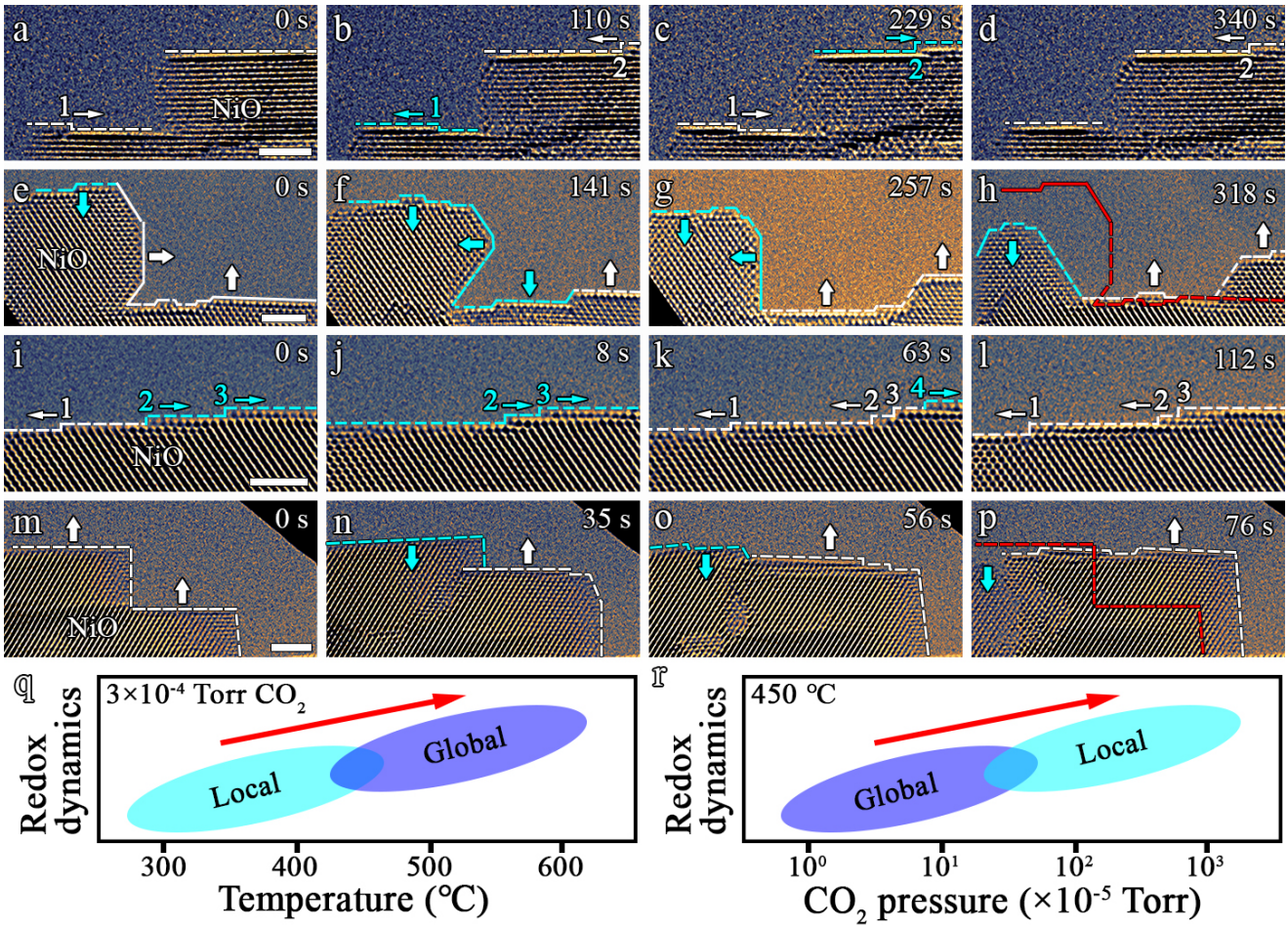

Figure 5. In-situ TEM imaging of the temperature and CO_2 pressure effect on NiO redox dynamics. **a-d** Local redox: simultaneous oxidation and reduction on the same facets at 300 °C and ≈ 3×10^{-4} Torr CO_2 (Supplementary Movie 8). **e-h** Global redox: oxidation and reduction on separate NiO facets at 450 °C and ≈ 3×10^{-4} Torr CO_2 (Supplementary Movie 9). The red dashed line in (h) is the superimposed trace of the surface position and profile of the oxide at t=0 s in (e). **i-l** Local redox: simultaneous oxidation and reduction on the same NiO facet at 450 °C and ≈ 3×10^{-2} Torr CO_2 (Supplementary Movie 10). **m-p** Global redox: NiO growth and reduction on separate facets at 600 °C and ≈ 3×10^{-4} Torr CO_2 (Supplementary Movie 11). The red dashed line in (p) is the superimposed trace of the surface position and profile of the oxide at t=0 s in (m). Scale bar, 2 nm **a-p**. **q, r** Temperature and pressure effects on the spatiotemporal redox dynamics of NiO, where "Local" means simultaneous NiO growth/reduction reactions on the same facets and "Global" refers to the competing NiO growth/reduction reactions on separated NiO grains.

The NiO growth requires the transport of Ni atoms to the growing step edges whereas the NiO reduction involves the transport of Ni atoms away from the receding step edges. As shown in Figs. 1-5, the CO_2-adsorption induced Ni oxidation occurs via an adatom process, in which the step-flow NiO growth takes place as a result of the surface diffusion of O and Ni adatoms, where O adatoms are supplied from dissociative adsorption of CO_2 molecules ($CO_2 \rightarrow CO + O$) whereas Ni adatoms are provided from the Ni substrate and reducing NiO in the

neighboring area. Conversely, the observed receding motion of atomic steps is induced by the reduction of NiO to Ni, where the adsorbed CO reacts with lattice O along the step edge to form CO_2. The surface desorption of the CO_2 molecule formed along the step edge is accompanied with the loss of lattice O, which therefore destabilizes the Ni atoms at the edge and leads to the Ni detachment from the step edge. Morphologically, this phenomenon appears similar to an etching process, but its origin is related to the loss of lattice O that results in the reduction NiO to Ni. Experimentally, the NiO $\rightarrow$ Ni reduction is confirmed by several mutually consistent phenomena from the in-situ TEM observations, including the presence of mobile Ni adatoms formed from the receding motion of atomic steps (Fig. S3), coordinated NiO growth with the supply of Ni adatoms from reducing NiO regions (Figs. 1-5), and the aggregation of Ni adatoms into a metallic-like Ni layer in the adjacent area of the same surface terrace, as indicated by the smaller interplanar spacing in the region marked by the red dashed oval in Fig. 3(k). Such oxide-reduction induced receding motion of atomic steps is also consistent with the microscopic processes underlying the reduction of Cu oxides (Cu_2O and CuO) to Cu adatoms in the H_2 atmosphere.[27,28] Meanwhile, our DFT calculations indicate that it is energetically more favorable for Ni adatoms attaching to a step edge to result in increased coordination than staying on the terrace (Fig. S2(a)). The calculated energy barrier for Ni adatoms hopping between fcc hollow sites via a minimum energy path passing the bridge site is ~ 0. 28 eV (Fig. S2(b)), indicating the high kinetic efficiency of the mass transport between oxidizing and reducing surface regions of the NiO islands. This involvement of the Ni transport can be further reflected from the temperature and CO_2 pressure effect on the spatiotemporal redox dynamics shown in Fig. 5, where the higher temperature results in more efficient surface diffusion of Ni atoms, thereby leading to the more global redox dynamics across the different surface regions. By contrast, the increase in CO_2 pressure leads to a higher surface density of adsorbed CO_2, which results in more local redox dynamics by capturing or trapping Ni adatoms.

The electron beam effects must be carefully examined when working with in-situ TEM observations. We perform both the “low-dose” and “blank-beam” experiments” to ensure that an intrinsic behavior is studied. By blanking the electron beam, simultaneous oxide growth and reduction still happens in “the dark” (Fig. S5). Additionally, low-magnification TEM imaging (Fig. 4) is performed at a significantly lower electron beam dose (810 e/Å^2 s) rate than the HRTEM imaging (8400 e/Å^2 s) in Figs. 1-3, and their mutual consistence confirms the

negligible electron beam effects. This is further verified by in-situ TEM observations of the oxidation of metallic Ni into NiO in a pure O_2 atmosphere (Figs. S6, S7), showing the monotonic NiO growth via the step-flow mechanism without experiencing any noticeable oxide decomposition under the same electron-beam irradiation condition as the CO_2 gas flow. Furthermore, our in-situ HRTEM imaging (Fig. S8) indicates that the NiO lattice is stable during vacuum annealing at 450 ℃, and the continuous electron beam irradiation does not induce noticeable oxide reduction, as confirmed from the negligible changes in the lattice contrast and the step-terrace surface morphology. Therefore, the observed competing oxidation and reduction is inherent and can be attributed to the dissociative CO_2 adsorption that results in adsorbed O and CO, where the adsorbed O is converted into the lattice O via the oxidation of Ni adatoms whereas the resulting CO serves as a reducing agent to react with lattice O and lead to the oxide reduction.

2.2 AP-XP, RGA and IR measurements

Ambient-pressure X-ray photoelectron spectroscopy (AP-XPS), residual gas analyzer (RGA) and infrared (IR) spectroscopy measurements are performed to further elucidate the reaction pathway derived from the in-situ TEM observations shown above. Same as the environmental TEM experiments, the AP-XPS, IR and RGA measurements also start from freshly cleaned Ni by H_2 annealing ($pH_2 = 1\times10^{-1}$ Torr) at T = 450 ℃ to remove native oxide. Fig. 6(a) illustrates the time-series O 1s XPS spectra, showing that the Ni surface is initially oxide-free and the subsequent CO_2 exposure results in growing intensity of the O 1s peak at the binding energy of 530.5 eV, which corresponds to lattice O in NiO. Fig. 6(b) presents the time evolution of the peak intensity of the O 1s spectra obtained during the CO_2 gas flow, which shows the gradually increased peak intensity without exhibiting noticeable intensity oscillation. The XPS measurements are performed under the condition of 450 ℃ and $\approx 1\times10^{-1}$ Torr CO_2, where the CO_2 pressure is an order of magnitude higher than the highest CO_2 pressure employed in the in-situ TEM observation (Fig. 5(i-l)). Based on the trend extrapolated from Fig. 5(r), increasing the CO_2 pressure leads to more localized redox dynamics, which cannot be probed by XPS because its large probed area (~ 300 μm) and long data acquisition time (~ 1 min) result in the temporal and spatial summation of the overall signals from the probed surface area. As a result, the ensemble average of a large surface area has washed out the uncorrelated oxidation and

reduction reaction elements at different surface regions. This also underscores the need of in-situ TEM observations (shown in Figs. 1-5) to probe the intrinsic kinetics of the gas-surface reactions by temporally and spatially resolving the local reaction dynamics.

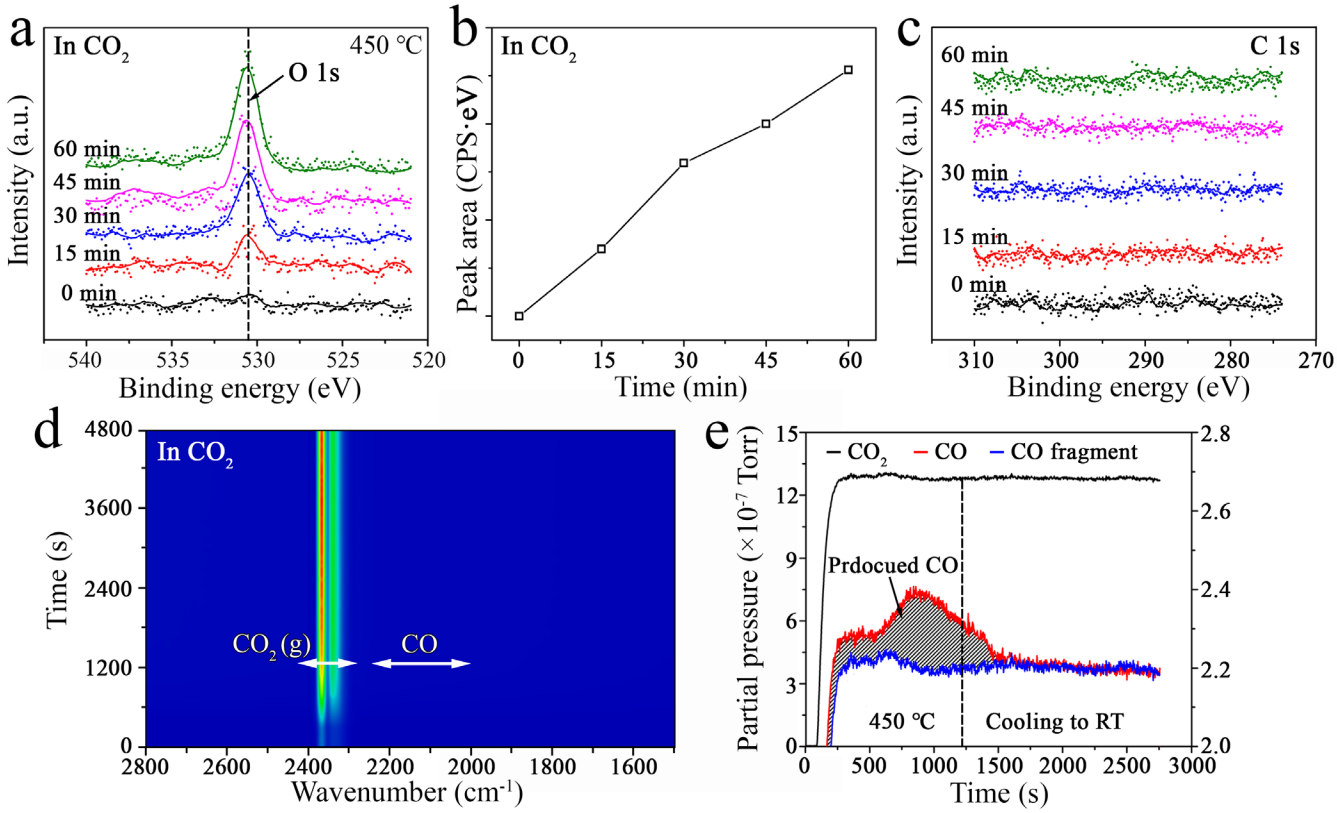

Fig. 6. AP-XPS, IR, and RGA measurements. **a-c** Time sequence and intensity evolution of O 1s and C 1s spectra acquired during the exposure of freshly cleaned Ni at 450 ℃ to 0.1 Torr of CO_2 gas flow. **d** Time-resolved IR measurements showing the absence of adsorbed CO_2 and CO (wavenumber range between 2250 and 2000 cm^{-1}), where the bright color bands correspond to the adsorption lines by gaseous CO_2. **e** Evolution of the partial pressure of CO_2 (black), total detected CO (red), and background CO (blue) measured by RGA.

Fig. 6(c) corresponds to coordinated XPS C 1s spectra obtained during the CO_2 flow, showing the absence of detectable intensity of C 1s signal. This indicates the extremely rapid dissociation reaction of $CO_2 \rightarrow CO + O(ad)$ and rapid surface desorption of CO. The lack of stably adsorbed CO_2 or CO is further confirmed by a flow-reactor system equipped with an IR spectrometer and a RGA setup. Time-resolved IR measurements (Fig. 6(d)) indicate the absence of adsorbed CO_2 and CO due to the facile dissociation of CO_2 and rapid desorption of the resulting CO at the elevated temperature, which corroborate well with the AP-XPS measurements (Fig. 6(a-c)). Fig.

6(e) illustrates the coordinated RGA results, showing the presence of gaseous CO (the grey shaded area in Fig. 6(e)) after flowing CO_2 gas at the elevated temperature, confirming the desorption of CO from the CO_2 dissociation. The RGA measurements also show that the gaseous CO amount drops to the background level (CO fragment) after cooling the Ni sample to room temperature, indicating that the elevated temperature is required to promote the CO_2 dissociation.

2.3 Atomistic insights into the competing oxidation and reduction reactions

The above in-situ TEM observations along with AP-XPS, IR and RGA measurements demonstrate the existence of competing oxide growth and shrinkage during the CO_2 induced Ni oxidation. The NiO shrinkage is induced by the presence of gaseous CO (resulting from the dissociative adsorption of CO_2) that leads to the oxide reduction. The surface reactions can be represented as follows:

$$\begin{array}{l} CO_2 \rightarrow CO(ad) + O(ad) \rightarrow O^{2-}(lattice) \\ \qquad\qquad\quad \downarrow \\ \qquad\qquad\quad CO(gas) + O^{2-}(lattice) \rightarrow CO_2 \end{array}$$

Primarily, CO_2 adsorbs onto the Ni surface and dissociates to CO and atomic O. The lack of C signal in the AP-XPS and IR measurements suggests the extremely rapid adsorption and desorption rates of CO_2 and CO molecules. As a result, no significant coverage of CO_2 and CO could build up to the level that can be detected experimentally. The in-situ HRTEM imaging (Figs. 1-3) clearly shows the step-flow oxide growth, which demonstrates an adatom mechanism of the oxidation process via surface diffusion of Ni and O adatoms onto the oxide growth front (step edges), where Ni adatoms are from the Ni substrate and O adatoms are supplied by dissociative CO_2 adsorption. Two further processes are the rapid desorption of adsorbed CO and the possibility of the removal of lattice O^{2-} by its reaction with CO molecules from the gas phase, the latter of which leads to the NiO reduction via the retraction motion of atomic steps, as shown from the above in-situ TEM observations.

To further substantiate the experimentally observed step-flow dynamics of the competing oxide growth and reduction, we employ DFT to elucidate the microscopic mechanisms by evaluating the adsorption energetics of CO_2 and CO at various surface sites. As shown in panel i of Fig. 7(a), we first consider CO_2 adsorption on bulk-terminated, perfect NiO(100). After considering all the C-Ni, O-Ni, and C-O coordination cases, CO_2 is found to

preferably adsorb in a monodentate configuration (in which the C is bound to the O atom) through the weak physisorption. This is reflected from the calculated adsorption of -0.03 eV, which is in the range of the physisorption. That is, adsorption energies of -0.01 ~ -0.1 eV correspond to the physical adsorption and the adsorption energies of -1 ~ -10 eV belong to chemisorption. It has been well established in the literature that NiO formed from Ni oxidation is intrinsically Ni-deficient with the existence of a small concentration of Ni vacancies.[29–31] As illustrated in panel ii of Fig. 7(a), our DFT calculation shows that the presence of a Ni vacancy makes CO_2 adsorption further unfavorable and results in spontaneous CO_2 desorption from the surface terrace. On the contrary, the presence of a Ni adatom (as supplied from the Ni substrate) makes the CO_2 adsorption favorable with the adsorption energy of –0.99 eV (panel iii of Fig. 7(a)) and facilitates the nucleation of a new atomic layer of NiO on the flat NiO surface. This is consistent with our in-situ TEM observations in Fig. 2(d-h), showing the layer-by-layer NiO nucleation along the side (100) facet. Along with the experimentally observed step-flow NiO growth, the lack of CO_2 adsorption for the flat surface terrace suggests preferred CO_2 adsorption along step edges. Indeed, our DFT calculations show that the CO_2 molecule preferentially adsorbs along the step edge with an adsorption energy of -1.31 eV, as shown in panel iv of Fig. 7(a). The CO_2 step-edge adsorption is still quite favorable (with the adsorption of -1.15 eV) even with the presence of a Ni vacancy along the step edge (panel v of Fig. 7(a)).

We then examine CO adsorption at various surface sites leading to NiO reduction. As shown in panel i of Fig. 7(b), CO on perfect NiO(100) is unstable and desorbs spontaneously from the surface. The presence of a Ni vacancy leads to a significant increase of the CO affinity with the NiO surface with an adsorption energy of -4.36 eV (panel ii of Fig. 7(b)). It can also be seen that the adsorbed CO directly bonds with the lattice O adjacent to the Ni vacancy. This results in the formation of a CO_2 molecule that tends to desorb from the surface, as evidenced by the upward relaxation of the lattice O from the surface. This is consistent with the in-situ TEM observations (Figs. 2 and 3), showing the formation of atomic pits on the flat terraces, where the presence of Ni vacancies is evidenced by significantly weakened lattice image contrast of topmost atomic layer. The surface pitting also results in the information of atomic steps that are found to be energetically favorable for CO adsorption (-1.09 eV) (panel iii, Fig. 7(b)). The presence of a Ni vacancy along the atomic step further promotes the step-edge CO adsorption with a significantly lower adsorption energy of -5.72 eV. As shown in panel iv of Fig. 7(b), this step-edge CO adsorption

results in the formation of a CO_2 molecule by bonding with the lattice O at the step edge. This is accordance with our experimental results (Figs. 1, 2), showing receding motion of atomic steps induced by CO adsorption induced NiO reduction.

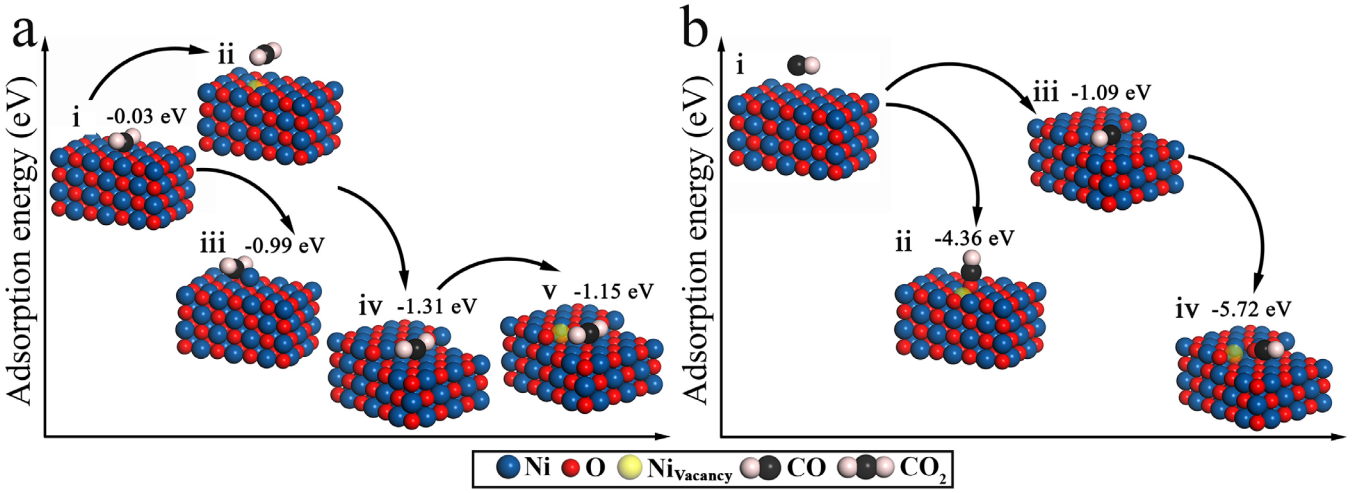

Figure 7. DFT modeling of competing redox reactions on Ni(100). **a** CO_2 adsorption at various surface sites for NiO growth, (i) perfect, buck-terminated NiO(100), (ii) the surface with a Ni vacancy, (iii) the surface with a Ni adatom, (iv) surface step, (v) surface step containing a Ni vacancy. **b**. CO adsorption at various surface sites for NiO reduction, (i) perfect NiO(100), (ii) the surface with a Ni vacancy, (iii) surface step, (iv) surface step containing a Ni vacancy.

Non-catalytic gas-solid reactions are usually assumed to occur irreversibly when being analyzed in conjunction to designing large-scale chemical reactions. By contrast, our results shown above demonstrate that this assumption is oversimplified for reactions even with a pure gaseous reactant. That is, although the feed gas of CO_2 favors the oxidation of Ni into NiO, the simultaneous presence of the gaseous reaction product (CO) can lead to appreciable reverse reaction in local areas because the solid is exposed to a mixture of the reactant and product gases. The reverse element of the reaction from the product gas slows down the overall rate of the conversion and should be taken into consideration because it is usually difficult to separate the product gas from the feed gas in a chemical reactor. Using the oxidation of metals as an example, Wagner theory is widely employed to explain the parabolic-type kinetics of the oxidation resulting from the control of the oxide growth by lattice or volume diffusion. However, deviations from the parabolic kinetics during the steady-state oxide scale growth period has frequently been observed. Several interpretations have been used to explain such deviations, including a phase-boundary process as the rate determining step of the reaction,[32,33] built-in electric field driven ionic diffusion,[34,35] doping effect

in the oxide scale,[36–39] and microstructure evolution effect on the oxide scale growth.[40–46] The reverse reaction is often ignored to explain the deviations from the parabolic kinetics of the scale oxide growth. As shown from our results of the CO_2 induced Ni oxidation, the reverse element of the reaction indeed exists and should be taken into account in order to understand the overall reaction rate.

Conclusions

We have provided direct evidence for the existence of simultaneously occurring forward and reverse reactions during the oxidation of Ni by CO_2. We have identified the atomic processes leading to the simultaneously occurring redox reactions. The oxidation reaction occurs via the preferential CO_2 adsorption along step edges that results in step-flow growth of NiO layers, and the presence of Ni atoms on the flat NiO surface promotes the nucleation of NiO layers. Simultaneously, the preferential step-edge adsorption of CO from the dissociative CO_2 adsorption results in the NiO reduction via the receding motion of the atomic steps, and the presence of Ni vacancies on the flat NiO surface facilitates the CO adsorption induced surface pitting that results in the formation of new atomic steps and thus further enhances the oxide reduction. The results provide mechanistic insight into the gas-surface reactions, which may find broader implication in tuning the interfacial reactions via controlling the composition of the gas reactants or atomic structure of the solid surface.

Experimental and modeling methods

In-situ environmental TEM experiments. Ni thin foils with a normal thickness (~ 50 nm) were prepared using Focused Ion Beam (FIB) lift-out techniques. To minimize potential surface damage and possible Ga contamination, a lower voltage (5 kV) and current (9 pA) of the Ga ion beam were used to perform the final surface trimming of the sliced sample. The Ni slice was loaded on a Mo Omniprobe Lift-out grid and further polished by a NanoMill TEM specimen preparation system with a low voltage (900 V) and current (80 pA) of Ar+ ions to remove surface damage and contamination. The as-prepared Ni surface was examined by EDX analyses, showing the absence of Ga contamination from the FIB process (see Fig. S9). Our environmental TEM experiments were performed with FEI Titan 80-300, equipped with an image aberration corrector and differential pumping apertures. The microscope has a spatial resolution of 0.8 Å in the high-resolution TEM mode.

Our in-situ TEM experiment encountered a two-step process. First, the Ni foil was annealed at ~ 450 °C and 5×10^{-3} Torr of H_2 gas flow in the sample region, which reduced any native Ni oxides to metallic Ni and generated tears and holes. The atomic structure and surface cleanliness of the as-prepared Ni surfaces were confirmed by HRTEM imaging, electron diffraction, and electron energy loss spectroscopy (see details in Fig. S10). The temperature and CO_2 pressure effects on the NiO redox dynamics were examined by two sets of in-situ TEM experiments: i) constant CO_2 pressure (3×10^{-4} Torr) while varying temperature from 300 °C to 600 °C, and ii) constant temperature (450 °C) while increasing CO_2 pressure from 4×10^{-5} Torr to 3×10^{-2} Torr. In-situ TEM observations of the CO_2 reaction with Ni were made in both planar and cross-sectional views. To ensure that we observed intrinsic behavior of the surface phenomena, an imaging protocol based on low-dose microscopy techniques was adopted to minimize the effects of electron beam irradiation, including performing focusing and crystal zone-axis orientation on an adjacent region of the specimen and then moving the specimen to the area of interest for TEM imaging.

The in-situ TEM experiments are performed using a Gatan heating holder. The Ni foil was firstly reduced in the TEM to remove native oxides at ~ 450 °C and 5×10^{-3} Torr of H_2 gas. The switch of the gas flow from H_2 to CO_2 resulted in the specimen drift, and it took ~ 5 min to stabilize the specimen. As a result, the Ni surface was

already oxidized into NiO islands under the CO_2 gas before in-situ TEM observations can be performed. It should be noted that metallic Ni regions were still available between NiO islands. Our in-situ TEM observations were focused on the oxidized regions, where the competing oxide growth and reduction reactions occurred.

AP-XPS and flow-reactor measurements. For cross-validating the in-situ TEM observations, complementary AP-XPS experiments were performed at the Center for Functional Nanomaterials at Brookhaven National Laboratory. The system is equipped with an XPS spectrometer (SPECS Phoibos 100 MCD analyzer), and a monochromatic Al Kα X-ray source (1486.6 eV, ~ 0.25 eV line width) focused on the sample to a spot size < 300 μm. The Ni foil was heated up by a laser heater at the backside of the sample holder. The AP-XPS equipped with multiple differential pumping apertures allows for gas pressure in the Torr range in the sample region while maintaining ultrahigh vacuum (UHV) conditions in the hemispherical analyzer. All spectra were collected at a takeoff angle of 20° between the surface and the electron analyzer optics of the XPS spectrometer. Binding energies in each spectrum were referred to the Fermi level for correction and XPS spectra were analyzed with the Voigt line shape and Shirley-type background. The line shape of a Gaussian/Lorentzian sum formula modified using an exponential tail function was introduced for accurate peak fitting and deconvolution. A flat Ni foil (Princeton Scientific Corp, purity = 99.9999%) was cut to a 1 cm × 1 cm square shape and fixed on the sample holder by spot welding. The Ni sample was firstly annealed at $pO_2 = 10^{-5}$ Torr oxygen gas at 450 ℃ for 20 min to burn out the carbon-containing contamination and then switch to 1 Torr of H2 gas flow for 30 min to remove any Ni oxide. The surface cleanliness was checked by XPS spectra until no obvious peaks showed up in O 1s and C 1s spectra. The flow-reactor measurements were carried out in an FTIR spectrometer (Thermo Nicolet 6700) equipped with a Harrick Praying Mantis™ high temperature reaction cell. An appropriate amount of Ni powder was loaded into the cell and firstly reduced by 20 vol% H_2 in He (20 mL min^{-1}) at 450 ℃ for 60 min, followed by an exposure to 10 vol% CO_2 in He (20 mL min^{-1}) at 450 ℃. The IR spectra were successively collected (32 scans) at a resolution of 4 cm^{-1}. The outlet species were continuously detected by a Stanford RGA setup (200 amu). To determine the 28 amu fragment from the product CO, the background of m/z=28 was measured with CO_2 purging at room temperature where no observable reaction occurred.

DFT calculations. DFT calculations were performed using the Vienna Ab initio Simulation Package (VASP) codes.[47,48] The exchange and correlation were described by the Perdew−Burke−Ernzerhof (PBE) exchange-correlation functional under generalized gradient approximation (GGA). The values of Hubbard parameters were U = 5 eV and J = 0 eV. The projector augmented-wave (PAW)[49,50] potential was used to describe the interaction between the ion and valence electrons, and the cut-off energy was set to be 500 eV, similar as the previous calculations.[51] In our calculations, the k-point grid within the Monkhorst-Pack scheme employed for the flat and stepped surfaces was 2×4×1. All the surface structures were fully relaxed by using the conjugate gradient method, until the forces on each atom were less than 0.015 eV/Å. Our calculated lattice parameter for bulk NiO is 4.17 Å. A periodically repeated six-layer slab was employed in our calculations for the flat surface, with the bottom three atom layers fixed at their bulk positions and the other layers to relax fully. The surface step was generated by removing some atomic columns in the topmost layer. Successive slabs are separated by a vacuum region of at least 15 Å to avoid interactions between slabs. We investigated the adsorption of both CO_2 and CO molecules at different sites of the NiO(100) surfaces. Additionally, the adsorption energies and diffusion energy barriers of Ni adatoms on the NiO surfaces were calculated. All the atomic structures are visualized using the Visualization for Electronic and Structure Analysis (VESTA).

ASSOCIATED CONTENT

Supporting Information.

Supporting information is available free of charge on the ACS publication website:

Sample preparation, Supplementary figures, and Supplementary in-situ TEM movies

AUTHOR INFORMATION

Corresponding Author

* gzhou@binghamton.edu.

‡ These authors contributed equally to the work

Notes

The authors declare no competing interests.

ACKNOWLEDGMENT

This work was supported by the U.S. Department of Energy, Office of Basic Energy Sciences, Division of Materials Sciences and Engineering under Award No. DE-SC0001135. This research used resources of the Center for Functional Nanomaterials and the Scientific Data and Computing Center, a component of the Computational Science Initiative, at Brookhaven National Laboratory, which is supported by the US Department of Energy, Office of Basic Energy Sciences, under Contract No. DE-SC0012704.

References

(1) Khoshandam, B.; Kumar, R. V.; Valipour, M. S.; Darzi, H. R. Modelling of Non-Catalytic Gas–Solid Reactions–Multicomponent Non-Equimolar Counter Diffusion of Gaseous Phase. *Miner. Process. Extr. Metall.* **2009**, *118* (2), 85–97.

(2) Frey, H.; Beck, A.; Huang, X.; Van Bokhoven, J. A.; Willinger, M.-G. Dynamic Interplay between Metal Nanoparticles and Oxide Support under Redox Conditions. *Science* **2022**, *376* (6596), 982–987.

(3) Huang, X.; Jones, T.; Fedorov, A.; Farra, R.; Copéret, C.; Schlögl, R.; Willinger, M. Phase Coexistence and Structural Dynamics of Redox Metal Catalysts Revealed by Operando TEM. *Adv. Mater.* **2021**, *33* (31), 2101772.

(4) He, Y.; Liu, J. C.; Luo, L.; Wang, Y. G.; Zhu, J.; Du, Y.; Li, J.; Mao, S. X.; Wang, C. Size-Dependent Dynamic Structures of Supported Gold Nanoparticles in CO Oxidation Reaction Condition. *Proc. Natl. Acad. Sci. U. S. A.* **2018**, *115* (30), 7700–7705.

(5) Vincent, J. L.; Crozier, P. A. Atomic Level Fluxional Behavior and Activity of CeO_2-Supported Pt Catalysts for CO Oxidation. *Nat. Commun.* **2021**, *12* (1), 1–13.

(6) LaGrow, A. P.; Lloyd, D. C.; Gai, P. L.; Boyes, E. D. In Situ Scanning Transmission Electron Microscopy of Ni Nanoparticle Redispersion via the Reduction of Hollow NiO. *Chem. Mater.* **2018**, *30* (1), 197–203.

(7) Amiri, A.; Ingram, G. D.; Bekker, A. V.; Livk, I.; Maynard, N. E. A Multi-Stage, Multi-Reaction Shrinking Core Model for Self-Inhibiting Gas–Solid Reactions. *Adv. Powder Technol.* **2013**, *24* (4), 728–736.

(8) Gómez-Barea, A.; Ollero, P. An Approximate Method for Solving Gas-Solid Non-Catalytic Reactions. *Chem. Eng. Sci.* **2006**, *61* (11), 3725–3735.

(9) Schmidt, L. D. *The Engineering of Chemical Reactions*; Oxford University Press, 1998.

(10) Ramachandran, P. A.; Doraiswamy, L. K. Modeling of Noncatalytic Gas-solid Reactions. *AIChE J.* **1982**, *28* (6), 881–900.

(11) Zhang, Z.; Shen, C.; Sun, K.; Jia, X.; Ye, J.; Liu, C. Advances in Studies of Structural Effect of the Supported Ni Catalyst for CO_2 Hydrogenation: From Nanoparticle to Single Atom Catalyst. *J. Mater. Chem. A* **2022** *10* (11), 5792-5812.

(12) Zhu, J.; Cannizzaro, F.; Liu, L.; Zhang, H.; Kosinov, N.; Filot, I. A. W.; Rabeah, J.; Brückner, A.; Hensen, E. J. M. Ni-In Synergy in CO_2 Hydrogenation to Methanol. *ACS Catal.* **2021**, *11* (18), 11371–11384.

(13) Vogt, C.; Groeneveld, E.; Kamsma, G.; Nachtegaal, M.; Lu, L.; Kiely, C. J.; Berben, P. H.; Meirer, F.; Weckhuysen, B. M. Unravelling Structure Sensitivity in CO_2 Hydrogenation over Nickel. *Nat. Catal.* **2018**, *1* (2), 127–134.

(14) Jalama, K. Carbon Dioxide Hydrogenation over Nickel-, Ruthenium-, and Copper-Based Catalysts: Review of Kinetics and Mechanism. *Catal. Rev. Sci. Eng.* **2017**, *59* (2), 95–164.

(15) Saeidi, S.; Najari, S.; Hessel, V.; Wilson, K.; Keil, F. J.; Concepción, P.; Suib, S. L.; Rodrigues, A. E. Recent Advances in CO_2 Hydrogenation to Value-Added Products — Current Challenges and Future Directions. *Prog. Energy Combust. Sci.* **2021**, *85*, 100905.

(16) Frontera, P.; Macario, A.; Ferraro, M.; Antonucci, P. Supported Catalysts for CO_2 Methanation: A Review. *Catalysts* **2017**, *7* (2), 59.

(17) Sharifianjazi, F.; Esmaeilkhanian, A.; Bazli, L.; Eskandarinezhad, S.; Khaksar, S.; Shafiee, P.; Yusuf, M.; Abdullah, B.; Salahshour, P.; Sadeghi, F. A Review on Recent Advances in Dry Reforming of Methane over Ni-and Co-Based Nanocatalysts. *Int. J. Hydrog. Energy* **2021**, 47 (100), 42213–42233.

(18) Schütze, M.; Quadakkers, W. J. Future Directions in the Field of High-Temperature Corrosion Research. *Oxid. Met.* **2017**, *87* (5), 681–704.

(19) Zhu, Q. Innovative Power Generation Systems Using Supercritical CO_2 Cycles. *Clean Energy* **2017**, *1* (1), 68–79.

(20) Yang, L.; Qian, H.; Kuang, W. Corrosion Behaviors of Heat-Resisting Alloys in High Temperature Carbon Dioxide. *Materials* **2022**, *15* (4), 1331.

(21) Yin, J.; Zheng, Q.; Peng, Z.; Zhang, X. Review of Supercritical CO_2 Power Cycles Integrated with CSP. *Int. J. Energy Res.* **2020**, *44* (3), 1337–1369.

(22) Zhou, G.; Yang, J. C. Initial Oxidation Kinetics of Copper (110) Film Investigated by in Situ UHV-TEM. *Surf. Sci.* **2003**, *531* (3), 359–367.

(23) Zhou, G.; Yang, J. C. Temperature Effect on the Cu_2O Oxide Morphology Created by Oxidation of Cu (001) as Investigated by in Situ UHV TEM. *Appl. Surf. Sci.* **2003**, *210* (3–4), 165–170.

(24) Zhou, G.; Yang, J. C. Initial Oxidation Kinetics of Cu (100), (110), and (111) Thin Films Investigated by in Situ Ultra-High-Vacuum Transmission Electron Microscopy. *J. Mater. Sci.* **2005**, *20* (7), 1684–1694.

(25) Luo, L.; Zou, L.; Schreiber, D. K.; Baer, D. R.; Bruemmer, S. M.; Zhou, G.; Wang, C.-M. In-Situ Transmission Electron Microscopy Study of Surface Oxidation for Ni-10Cr and Ni-20Cr Alloys. *Scr. Mater.* **2016**, *114*, 129–132.

(26) Zhang, H.; Luo, L.; Chen, X.; Zhou, G. Tailoring the Formation of Textured Oxide Films via Primary and Secondary Nucleation of Oxide Islands. *Acta Mater.* **2018**, *156* (1), 266–274.

(27) Chen, X.; Wu, D.; Zou, L.; Yin, Q.; Zhang, H.; Zakharov, D. N.; Stach, E. A.; Zhou, G. In Situ Atomic-Scale Observation of Inhomogeneous Oxide Reduction. *Chem. Commun.* **2018**, *54* (53), 7342–7345.

(28) Sun, X.; Wu, D.; Zhu, W.; Chen, X.; Sharma, R.; Yang, J. C.; Zhou, G. Atomic Origin of the Autocatalytic Reduction of Monoclinic CuO in a Hydrogen Atmosphere. *J. Phys. Chem. Lett.* **2021**, *12* (39), 9547–9556.

(29) Luo, L.; Su, M.; Yan, P.; Zou, L.; Schreiber, D. K.; Baer, D. R.; Zhu, Z.; Zhou, G.; Wang, Y.; Bruemmer, S. M. Atomic Origins of Water-Vapour-Promoted Alloy Oxidation. *Nat. Mater.* **2018**, *17* (6), 514–518.

(30) Roberts, M. W.; Smart, R. S. C. The Defect Structure of Nickel Oxide Surfaces as Revealed by Photoelectron Spectroscopy. *J. Chem. Soc., Faraday Trans. 1* **1984**, *80* (11), 2957–2968.

(31) Cho, D.-Y.; Song, S. J.; Kim, U. K.; Kim, K. M.; Lee, H.-K.; Hwang, C. S. Spectroscopic Investigation of the Hole States in Ni-Deficient NiO Films. *J. Mater. Chem. C* **2013**, *1* (28), 4334–4338.

(32) Birks, N.; Meier, G. H.; Pettit, F. S. *Introduction to the High Temperature Oxidation of Metals*; Cambridge university press, 2006.

(33) Netzer, F. P. Interfacial Oxide Layers at the Metal-Oxide Phase Boundary. *Surf. Rev. Lett.* **2002**, *9* (03n04), 1553–1563.

(34) Cai, N.; Zhou, G.; Müller, K.; Starr, D. E. Temperature and Pressure Dependent Mott Potentials and Their Influence on Self-Limiting Oxide Film Growth. *Appl. Phys. Lett.* **2012**, *101* (17), 171605.

(35) Cai, N.; Zhou, G.; Müller, K.; Starr, D. E. Tuning the Limiting Thickness of a Thin Oxide Layer on Al(111) with Oxygen Gas Pressure. *Phys. Rev. Lett.* **2011**, *107* (3), 1–4.

(36) Ghadami, F.; Sabour Rouh Aghdam, A.; Ghadami, S. A Comprehensive Study on the Microstructure Evolution and Oxidation Resistance of Conventional and Nanocrystalline MCrAlY Coatings. *Sci. Rep.* **2021**, *11* (1), 1–21.

(37) Nguyen, T. D.; Xie, Y.; Ding, S.; Zhang, J.; Young, D. J. Oxidation Behavior of Ni-Cr Alloys in CO_2 at 700 °C. *Oxid. Met.* **2017**, *87* (5–6), 605–616.

(38) Oleksak, R. P.; Tylczak, J. H.; Carney, C. S.; Holcomb, G. R.; Doğan, Ö. N. High-Temperature Oxidation of Commercial Alloys in Supercritical CO_2 and Related Power Cycle Environments. *JOM* **2018**, *70* (8), 1527–1534.

(39) Pint, B. A.; Brese, R. G.; Keiser, J. R. Effect of Pressure on Supercritical CO_2 Compatibility of Structural Alloys at 750 °C. *Mater. Corros.* **2017**, *68* (2), 151–158.

(40) Peraldi, R.; Monceau, D.; Pieraggi, B. Correlations between Growth Kinetics and Microstructure for Scales Formed by High-Temperature Oxidation of Pure Nickel. II. Growth Kinetics. *Oxid. Met.* **2002**, *58* (3–4), 275–295.

(41) Geers, C.; Panas, I. Impact of Grain Boundary Density on Oxide Scaling Revisited. *Oxid. Met.* **2019**, *91* (1–2), 55–75.

(42) Xie, Y.; Zhang, J.; Young, D. J. Temperature Effect on Oxidation Behavior of Ni-Cr Alloys in CO_2 Gas Atmosphere. *J. Electrochem. Soc.* **2017**, *164* (6), C285–C293.

(43) Unutulmazsoy, Y.; Merkle, R.; Fischer, D.; Mannhart, J.; Maier, J. The Oxidation Kinetics of Thin Nickel Films between 250 and 500 °C. *Phys. Chem. Chem. Phys.* **2017**, *19* (13), 9045–9052.

(44) Huang, C. L.; Weng, W. L.; Liao, C. N.; Tu, K. N. Suppression of Interdiffusion-Induced Voiding in Oxidation of Copper Nanowires with Twin-Modified Surface. *Nat. Commun.* **2018**, *9* (1), 340.

(45) Zhu, Q.; Pan, Z.; Zhao, Z.; Cao, G.; Luo, L.; Ni, C.; Wei, H.; Zhang, Z.; Sansoz, F.; Wang, J. Defect-Driven Selective Metal Oxidation at Atomic Scale. *Nat. Commun.* **2021**, *12* (1), 6–13.

(46) Kim, S. J.; Kim, Y. I.; Lamichhane, B.; Kim, Y. H.; Lee, Y.; Cho, C. R.; Cheon, M.; Kim, J. C.; Jeong, H. Y.; Ha, T.; Kim, J.; Lee, Y. H.; Kim, S. G.; Kim, Y. M.; Jeong, S. Y. Flat-Surface-Assisted and Self-Regulated Oxidation Resistance of Cu(111). *Nature* **2022**, *603* (7901), 434–438.

(47) Kresse, G.; Furthmiiller, J. Efficiency of Ab-Initio Total Energy Calculations for Metals and Semiconductors Using a Plane-Wave Basis Set. *Comput. Mater. Sci.* **1996**, *6* (1), 15-50.

(48) Kresse, G.; Furthmü, J. Efficient Iterative Schemes for Ab Initio Total-Energy Calculations Using a Plane-Wave Basis Set. *Phys. Rev. B* **1996**, *54* (16), 11169-11186.

(49) Perdew, J. P.; Chevary, J. A.; Vosko, S. H.; Jackson, K. A.; Pederson, M. R.; Singh, D. J.; Fiolhais, C. Atoms, Molecules, Solids, and Surfaces: Applications of the Generalized Gradient Approximation for Exchange and Correlation. *Phys. Rev. B* **1992**, 46 (11), 6671-6687.

(50) Kresse, G.; Joubert, D. From Ultrasoft Pseudopotentials to the Projector Augmented-Wave Method. *Phys. Rev. B* **1999**, *59* (3), 1758-1775

(51) Wu, D.; Zhu, Y.; Shan, W.; Wang, J.; Liu, Q.; Zhou, G. Revealing an Intermediate Cu-O/OH Superstructure on Cu(110). *J. Phys. Chem. Lett.* **2022**, *13* (10), 2396-2403